



Article

Geometry Effect on Microstructure and Mechanical Properties in Laser Powder Bed Fusion of Ti-6Al-4V

Juri Munk ^{1,*} , Eric Breitbarth ² , Tobias Siemer ¹, Norbert Pirch ¹ and Constantin Häfner ^{1,3}

¹ Fraunhofer Institute for Laser Technology ILT, Steinbachstraße 15, 52074 Aachen, Germany; siemer-t@gmx.de (T.S.); norbert.pirch@ilt.fraunhofer.de (N.P.); constantin.haefner@ilt.fraunhofer.de (C.H.)

² Institute of Materials Research, German Aerospace Center (DLR), Linder Höhe, 51147 Cologne, Germany; eric.breitbarth@dlr.de

³ Chair for Laser Technology LLT, RWTH Aachen University, Steinbachstraße 15, 52074 Aachen, Germany

* Correspondence: juri.munk@ilt.fraunhofer.de

Abstract: Laser Powder Bed Fusion (LPBF) of Ti-6Al-4V enables the manufacturing of complex parts for lightweight applications. The emerging microstructure in the LPBF process and thus the mechanical properties are defined by the thermal cycles, which are locally variable for complex geometries. Predictions of local mechanical properties by simulation would reduce the development time of new applications drastically but are today not possible on part scale, so new part applications must be qualified experimentally at great effort. In this study, representative geometry sections were transferred into a simplified sample shape to mechanically characterize different geometry-dependent microstructures. In areas exposed to comparatively increased heat input over time, a lamellar $\alpha + \beta$ microstructure with β fraction up to 20% was measured in contrast to the common martensitic α' microstructure of LPBF-manufactured Ti-6Al-4V, resulting in reduced tensile strength and fatigue life. For the first time, a correlation was successfully established between ultimate tensile strength of multiple geometries and the corresponding temperature–time cycles. With reduced computational effort by use of simplifying assumptions in the simulation, this correlation model can theoretically be applied to the part level. This work has laid the foundation for the simulation-based prediction of mechanical properties for entire parts manufactured with LPBF.

Keywords: additive manufacturing (AM); laser powder bed fusion (LPBF); PBF-LB/M; Ti-6Al-4V; thermal history; intrinsic heat treatment; martensite decomposition; material characterization; thermal simulation



Citation: Munk, J.; Breitbarth, E.; Siemer, T.; Pirch, N.; Häfner, C. Geometry Effect on Microstructure and Mechanical Properties in Laser Powder Bed Fusion of Ti-6Al-4V. *Metals* **2022**, *12*, 482. <https://doi.org/10.3390/met12030482>

Academic Editors: Katrin Wudy and Peter Mayr

Received: 28 January 2022

Accepted: 10 March 2022

Published: 12 March 2022

Publisher's Note: MDPI stays neutral with regard to jurisdictional claims in published maps and institutional affiliations.



Copyright: © 2022 by the authors. Licensee MDPI, Basel, Switzerland. This article is an open access article distributed under the terms and conditions of the Creative Commons Attribution (CC BY) license (<https://creativecommons.org/licenses/by/4.0/>).

1. Introduction

Laser Powder Bed Fusion (LPBF) of Ti-6Al-4V offers considerable potential for lightweight applications. Combined with advanced design approaches such as topology optimization significant weight reduction is achievable with LPBF, such as 19–63% in the study by [1] with four aerospace use cases. The lightweight design is often associated with complex part geometries. This contrasts with the fact that primitive geometries such as cubes or cylinders are commonly used to characterize the microstructure and mechanical properties of LPBF-manufactured parts, as these simplifications do not represent the real emerging microstructure in a complex part [2,3]. The common microstructure that evolves in the LPBF process of Ti-6Al-4V is the martensitic α' phase due to a cooling rate of approx. 10^5 °C/s [4,5]. However, if the geometry differs from that of a primitive body a different microstructure can emerge, because on the one hand the cooling rates and on the other hand the subsequent temperature cycles (thermal history) can be significantly different from those of a full sample due to the neighboring traces in the same and especially in the subsequent layers. This influence of the traces can generally be observed in several additive manufacturing (AM) processes, not only LPBF. For Direct Energy Deposition (DED) of Ti-6Al-4V where traces are generally larger than in LPBF it was shown that

between different track layouts and load directions variations are existent in compressive strength in the range of 6% from 1794 MPa (parallel tracks) to 1910 MPa (vertical tracks) beside variations of other mechanical properties [6]. Additionally, in the case of a rapidly increasing exposure area in the build-up direction (e.g., downskin areas) heat accumulation can occur in AM processes and increase the mean temperature in the following thermal history. Compared to the build-up of a uniform body of constant cross section along the build direction, the heat from the weld pool can only be dissipated to a reduced amount via the comparatively smaller geometry cross sections below, leading to increased thermal input at this specific area. In [3] this effect results in an $\alpha + \beta$ microstructure with β phase fraction of 4–6% in downskin areas of a complex LPBF-manufactured part instead of the common $\sim 100\%$ α' phase.

The observed effect is called intrinsic heat treatment (IHT) and can also be existent for primitive sample geometries to a lesser extent in LPBF, influenced by the build height of the sample. It was found that in contrast to a martensitic top layer (α'), in the center region of the sample fine α lamellae with thickness 100–400 nm are existent, embedded in thin β layers of ~ 50 nm thickness. The martensitic top layer is explained by the fact that no following layers are added in this region, leading to a missing IHT and therefore leaving the initial α' microstructure that has emerged in the LPBF process in his original state, defined by the cooling rate. The gradation of the microstructure over build height is also confirmed by the hardness profile. Thus, a ~ 50 HV higher hardness is measured in the top layer compared to the underlying area, which has experienced IHT [7].

Investigations on post heat treatment of LPBF-manufactured Ti-6Al-4V with initial α' microstructure such as in [8] show that decomposition of α' starts from a temperature of 400 °C and proves that IHT is the main driver for the $\alpha' \rightarrow \alpha + \beta$ transformation. Variations in thermal history and local cooling rate with the corresponding changes in microstructure influence the mechanical properties of Ti-6Al-4V as shown in [9]. Thus, it can be stated that the geometry effect in LPBF of Ti-6Al-4V is a crucial factor for performance of structurally loaded part applications.

Established simulation methods for predicting the microstructure in the LPBF process, such as phase field models or cellular automata, are able to simulate microstructural properties below or at grain scale but are computationally intensive because several complex physical processes are simulated simultaneously and therefore cannot be applied on part scale with reasonable effort [10,11]. In [12], a semi-analytical heat conduction model was used to quantify the heat transfer as a function of part geometry and scan pattern for electron beam melting (EBM) of Ti-6Al-4V and the modeled cooling rate was correlated successfully with measured values of beta grain width but the investigated geometries (cube vs. bar) are not derived from characteristic geometrical features of real complex parts. Focusing on the level of single LPBF melt tracks, in [13] a model was applied to predict the thermal gradients for multilayer LPBF part sections at a defined location and to correlate them with experimentally determined characteristics on the formation and orientation of the martensitic α' phase and the prior β grains, but with an investigated scale that is also well below part dimension. In LPBF manufacturing of single Ti-6Al-4V struts of different thicknesses (0.4–1.4 mm), a geometry influence on the cooling condition in terms of the resulting relative density is observed [14], although the relative density values with a maximum of 98.1% is significantly below currently achievable values, limiting the significance of the study on geometry effect. In addition to the previously mentioned studies, there are also investigations on the geometry effect in LPBF manufacturing of other metallic alloys such as 17-4 stainless steel [15], 316L [16], or nickel-based super alloy IN718 [17,18]. In the unique LPBF part-scale study of [18], the thermal history, melt pool size, precipitations and primary dendrite arm spacing were simulated for a 70 mm tall part made of IN718 and successfully correlated with experimentally determined microstructural properties and in situ temperature measurements. Even though no significant geometry influence on the microstructure was identified for IN718 in this study, because of the fact that microstructure-defining precipitations are not influenced enough by the chosen part

geometry, the approach with combined in situ temperature measurement may be useful for investigations of the geometry effect with Ti-6Al-4V. The recently published study by [19] is the closest to a part-scale microstructure prediction model in LPBF of Ti-6Al-4V. In this study, a data-driven more efficient approach in terms of computational resources compared to conventional simulation models was adopted, using physically motivated parameters derived from experimental transient thermal data sets to simulate the phase distribution. The model is suitable for generating continuous-cooling transformation (CCT) as well as time-temperature transformation (TTT) diagrams, but was validated on part-scale at this stage only on the basis of a quenching test and not for the LPBF process with its complex thermal cycles.

To summarize, today there is no method to quantify the geometry effect on local microstructure and mechanical properties on the whole part scale of LPBF-manufactured parts with reasonable computational effort, which is why exaggerated high safety factors are used for additively manufactured parts and time-consuming test bench experiments are carried out for mechanical characterization. Precise knowledge of the geometry effect would allow exploiting significant design potential and drastically reduce the development effort for new applications. Moreover, post heat treatments could be saved if the microstructure can be predicted with sufficient accuracy after the LPBF process. This work aims at a better understanding of how part geometry influences the local microstructure and mechanical properties of LPBF-made Ti-6Al-4V. Furthermore, for the first time, material properties at selected geometry features are successfully correlated with thermal history simulations that represent a good approximation of intrinsic heat treatment and are more efficient than any other state of the art simulation methods and therefore theoretically applicable on part scale to create the basis for a prediction model.

2. Materials and Methods

The methodological approach of this work is shown schematically in Figure 1.

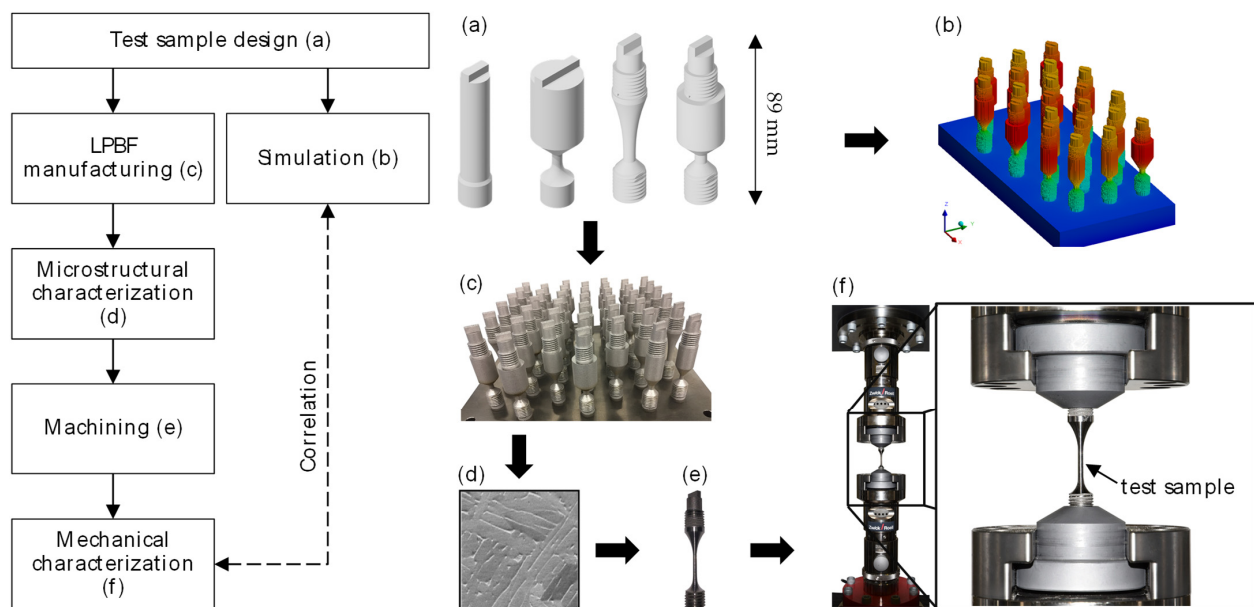


Figure 1. Methodology to determine the geometry effect on material properties and correlation with simulation results, (a) exemplary sample geometries with a varied cross-sectional area, (b) LPBF process thermal simulation of sample manufacturing, (c) exemplary LPBF-manufactured samples, (d) exemplary microstructure at investigation point in manufactured sample, (e) machined sample with uniform cross section for mechanical testing, (f) sample installed in tensile testing machine.

To determine the geometry effect on the material properties, initially, suitable sample geometries were developed, which should provide different thermal histories based on their differences in cross-sectional areas (a). The samples were then manufactured by LPBF (c) and microstructural investigations were performed on selected ones (d). Samples were machined into test shapes (e) to determine mechanical properties with static and dynamic mechanical testing (f). The LPBF process of the experimentally investigated sample geometries was simulated (b) to generate numerical parameters that were correlated with the mechanical properties to provide the basis for a predictive model.

2.1. Test Sample Design

A methodology was developed to determine the geometry effect on material properties at a specific location. For microstructure and fatigue testing, the geometries Geo-A and Geo-B were selected (Figure 2) to provide two contrary cases in terms of the cross section rate of change during the build process. Evaluation point P marks the location where the material properties were determined.

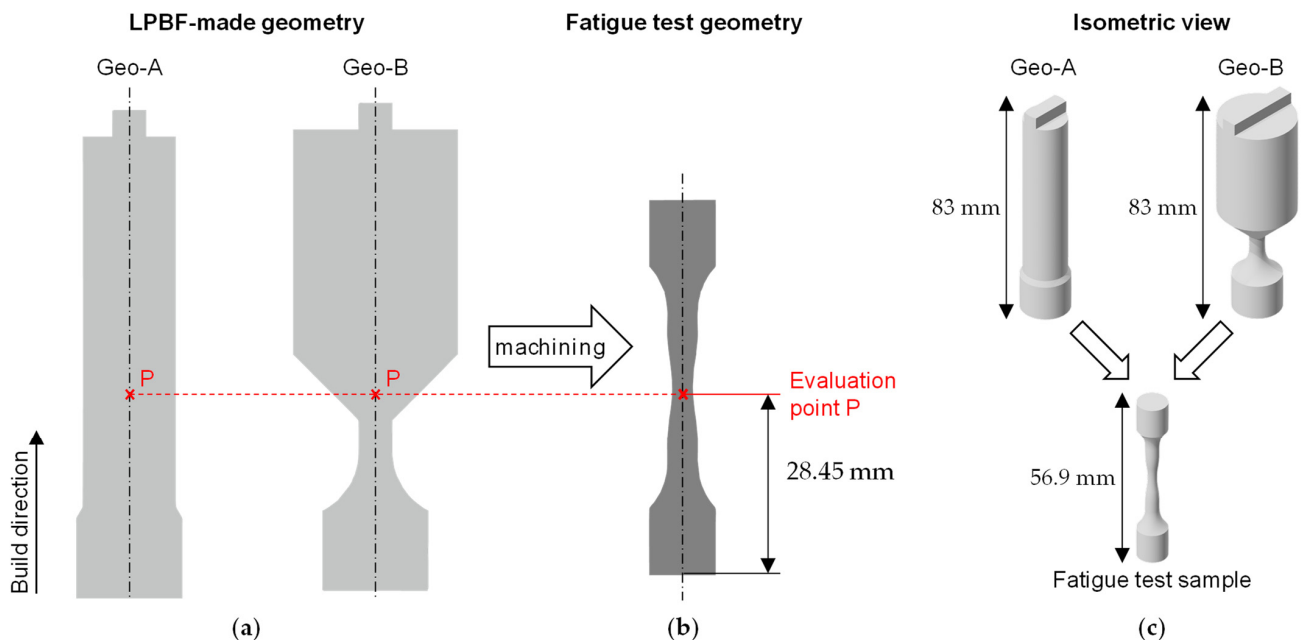


Figure 2. Methodology for local evaluation of geometry effect on microstructure and fatigue strength at evaluation point P, (a) LPBF-made geometry Geo-A and Geo-B, (b) Uniform fatigue test geometry after machining of Geo-A and Geo-B, (c) Isometric view of sample designs in LPBF-made condition and after machining in fatigue test geometry.

The LPBF-made geometry of Geo-A (Figure 2a, left) is characterized by an almost constant cross section course, whereas Geo-B (Figure 2a, right) provides a narrow cross section followed by a 45°-angled transition to an increased diameter. For fatigue testing, both LPBF-made geometries were machined to exactly the same fatigue test geometry (Figure 2b) in order to investigate solely the geometry influence in the LPBF process on the emerging microstructure, without the sample shape having any influence on the testing procedure, e.g., due to notch effects.

To quantify the geometry effect on the mechanical properties with a larger database, 21 geometry variants were developed to gain mechanical data from tensile test. In detail, according to Figure 3a the small diameter d , the large diameter D and, for the samples Geo-a to Geo-r, the overhang angle δ were varied according Table 1.

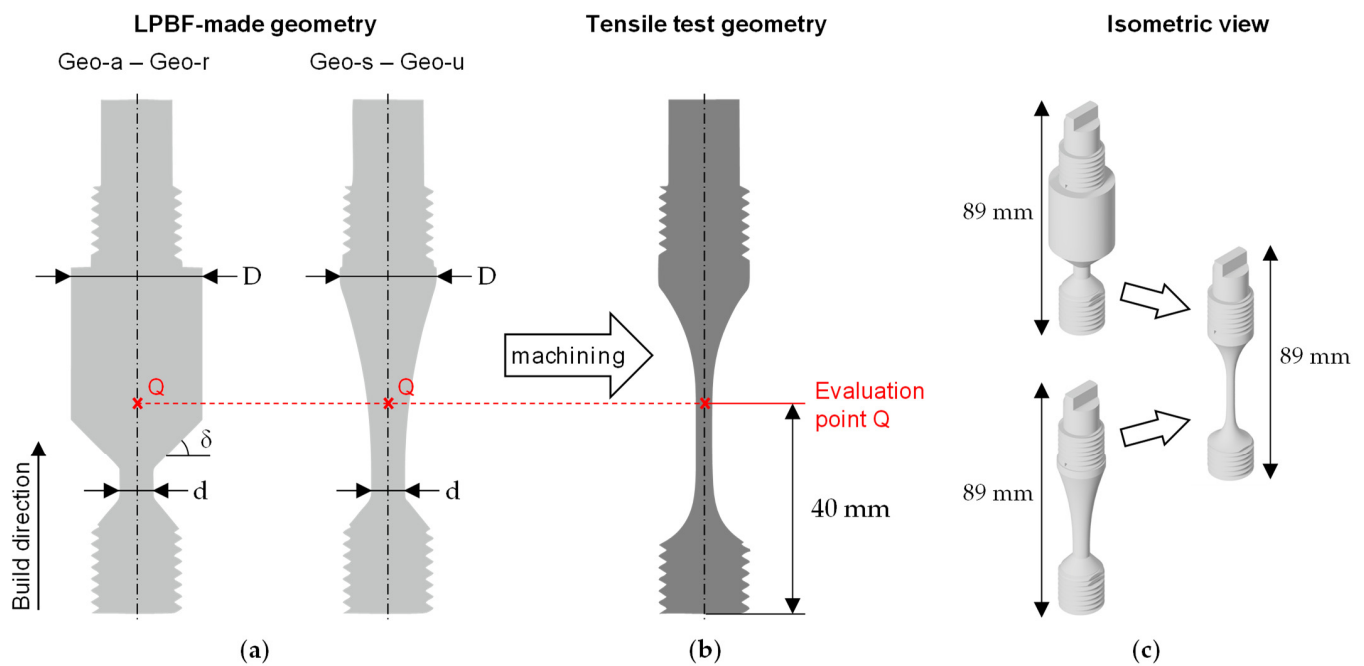


Figure 3. Methodology for local evaluation of geometry effect on tensile strength at evaluation point Q, (a) LPBF-made geometry with variation of D, d, δ for Geo-a–Geo-r and D, d for Geo-s–Geo-u (b) Uniform tensile test geometry after machining, (c) Isometric view of sample designs in LPBF-made condition and after machining in tensile test geometry.

Table 1. Geometry variants of tensile test samples.

Geometry variant, Geo-	a	b	c	d	e	f	g	h	i	j	k	l	m	n	o	p	q	r	s	t	u						
Small diameter, d (mm)	4			5			6			4			5			6			4			5			6		
Large diameter, D (mm)	17	20	23	17	20	23	17	20	23	17	20	23	17	20	23	17	20	23	17	20	23	17	20	23	17	20	23
Overhang angle, δ (°)	45												60														

As displayed in Figure 3a, Geo-a–Geo-r are characterized by a narrow section with small diameter d, followed by a faster increasing cross-sectional area than Geo-s–Geo-u, to provoke an increased thermal input. All LPBF-made samples were machined into a uniform tensile test geometry (Figure 3b). The sample cross section was smallest at the evaluation point Q to test the local microstructure in the tensile test at this specific point.

2.2. LPBF Manufacturing and Machining

Build job preparation was performed using Magics 24 software (Materialise NV, Leuven, Belgium). All samples were additively manufactured on the LPBF system SLM280 HL Twin (SLM Solutions Group AG, Lübeck, Germany) using the build strategy “Ti_SLM_MBP3.0_60_CE2_400W_Stripes_V1.2” with a laser beam diameter of 80 μ m. Hatch process parameters are shown in Table 2. Contour parameters are not relevant as all test samples were machined before testing.

Table 2. LPBF process parameters for sample manufacturing (hatch).

Laser Power, P_L (W)	Scanning Speed, v_s (mm/s)	Hatch Distance, Δy_s (μ m)	Layer Thickness, D_s (μ m)
350	1100	120	60

Ti-6Al-4V grade 5 powder from the manufacturer Carpenter Additive with the particle size distribution 15–45 μ m was used. The geometry variants for microstructure and fatigue

testing (Geo-A, Geo-B) and tensile testing (Geo-a–Geo-u) were manufactured in three build jobs each, with randomized platform positions of the geometry variants. For Geo-A and Geo-B, 12 samples were manufactured each. The microstructure was analyzed at one sample per geometry variant and fatigue testing was performed using nine samples of Geo-A and ten samples of Geo-B. For tensile testing of Geo-a–Geo-u, six samples per geometry variant were manufactured. In the LPBF sample manufacturing process, recoating was performed in both directions with a soft polymer recoater (Aixway3D GmbH, Aachen, Germany) at a recoating speed of 600 l/min (machine unit). A soft recoater was used because overhang angles of down to 45° without support structures were manufactured for some sample geometries. In this way, build job failures should be prevented that otherwise could have resulted from part deformation out of the powder bed followed by a recoater crash. The process pressure was set to 30 mbar and the gas pump setting was 80%.

2.3. Microstructural Characterization

A scanning electron microscope (SEM) Zeiss Gemini FE-SEM 1540XB (Carl Zeiss Microscopy GmbH, Jena, Germany) was used for the determination of the elemental distribution by energy-dispersive X-ray spectroscopy (EDS) analysis at acceleration voltage of 20 kV. For the optical determination of the phase fractions, the SEM system FEI XL30 FEG (FEI Company, Hillsboro, OR, USA) was used in backscattered electron (BSE) mode with acceleration voltage 15 kV. The captured images were evaluated with the Fiji plugin Weka Segmentation (The University of Waikato, Hamilton, New Zealand) to determine the phase fractions.

2.4. Machining

All LPBF-manufactured samples for mechanical testing were machined to the test geometry, displayed in Figures 2b and 3b. For this, turning was performed using a DNMG15040-SF1105 insert (Sandvik Coromant US, Mebane, NC, USA) at cutting velocity $v_c = 80$ m/min and feed per revolution $f_n = 0.1$ mm/r. Additionally, for fatigue samples of Geo-A and Geo-B grinding with grit 240, 400 and 1200 was performed followed by polishing with Autosol (Dursol Fabrik Otto Durst GmbH & Co. KG, Solingen, Germany) at 2400 rpm. No heat treatment was performed.

2.5. Mechanical Characterization and Fracture Surface Evaluation

Tensile testing was carried out by use of a ZwickRoell AllroundLine Z250 SN system with laserXtens software version 3.13.0.1 (Zwick Roell Group, Ulm, Germany) at room temperature with the samples clamped by threads. Fatigue tests were performed under axial tensile loading using an Amsler resonance testing machine (Alfred J. Amsler & Co., Schaffhausen, Switzerland) with a maximal load capacity of 20 kN. The load ratio R was 0.1 and the test frequency was about 90 Hz. In the long-life fatigue regime, the tests were stopped at an ultimate number of $1E7$ cycles and the sample was then evaluated as a runout. The fracture surfaces of fatigue samples were analyzed with an VHX-6000 optical microscope (Keyence Corporation, Osaka, Japan). According to Figure 4, crack initiation was classified into either (a) from a gas pore that evolved as a LPBF-processed-induced defect or (b) crack initiation at solid material. From preliminary investigations, it is known that the average part density (measured optically at cross sections of $10\text{ mm} \times 10\text{ mm} \times 10\text{ mm}$ cubic samples) is 99.99% (Figure 4c) for the given LPBF machine and process parameters setup. The observed pores correspond in size approximately to the defects observed on fracture surfaces (Figure 4a) and are supposed to have been created by keyholing as their size and morphology are similar to those that are experimentally observed in [20] where process parameters of a similar range were used ($P_L = 300\text{ W}$, $v_s = 1000\text{ mm/s}$). By excluding all samples of category (a), only those samples are evaluated in which the microstructure with the respective phase distribution was tested to failure. In this way, the geometry effect on fatigue strength was investigated independently from other influences.

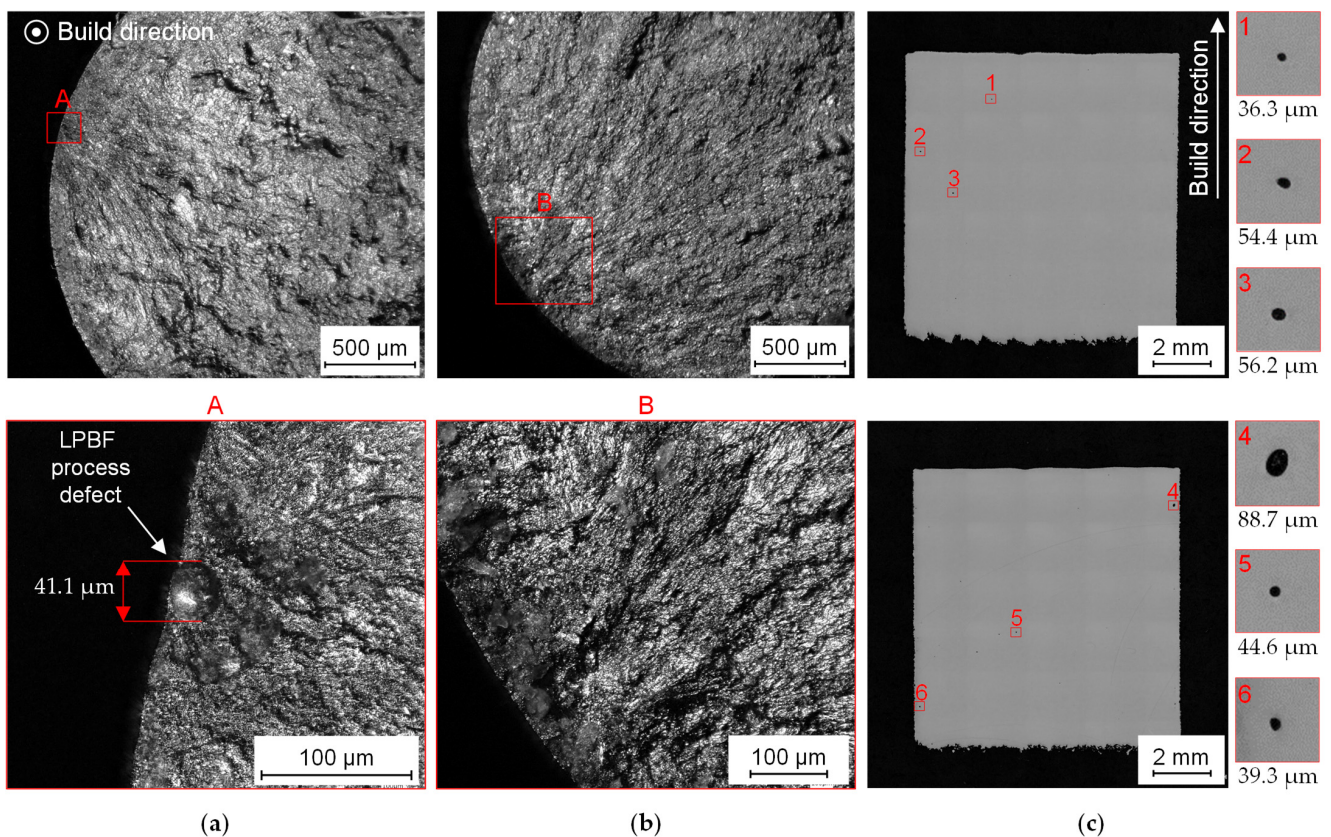


Figure 4. Fracture surface of two fatigue samples with crack initiation (a) at a gas pore as an LPBF process defect with detail view in A and (b) at solid material with detail view in B; Microscopical image of cross section of 10 mm × 10 mm × 10 mm cubic samples for optical density evaluation with indicated dimensions of six characteristic pores (1–6) in detail views (c).

2.6. Thermal Simulation and Correlation

Transient thermal LPBF process simulations of the tensile test samples build job (Geo-a–Geo-u) were performed with Ansys Workbench Additive 2020 R2 (ANSYS Inc, Canonsburg, PA, USA) using the super layer approach. In this process, element layers with a multiple thickness of the real layer thickness (super layers) are built up on top of each other according to the element-birth method. All elements of the super layer are initially at melting temperature immediately after formation and are cooled in a defined number of substeps before applying the next layer according to the inter layer time, which is defined by the scanning duration and the duration of the recoating process. The build job shown in Figure 5 was simulated as a half model by taking symmetry of the build job layout into account. A hex mesh with SOLID70 elements of size 0.6 mm, corresponding to 10 times the layer thickness, and five substeps per simulated super layer were used. Recoating time was set to 8.39 s according to experimental measurement. The platform temperature was set to 90 °C, which is the measured mean value in the layer range around the evaluation point Q at build time between 8000 and 10,300 s. To correlate simulation results with experimental results from tensile test, nodal solutions of temperature over build time were extracted from the cut plane at z-height of Evaluation Point Q that fit in a circle of diameter 3 mm (Figure 5–Detail A) representing the force-loaded cross section in the tensile test.

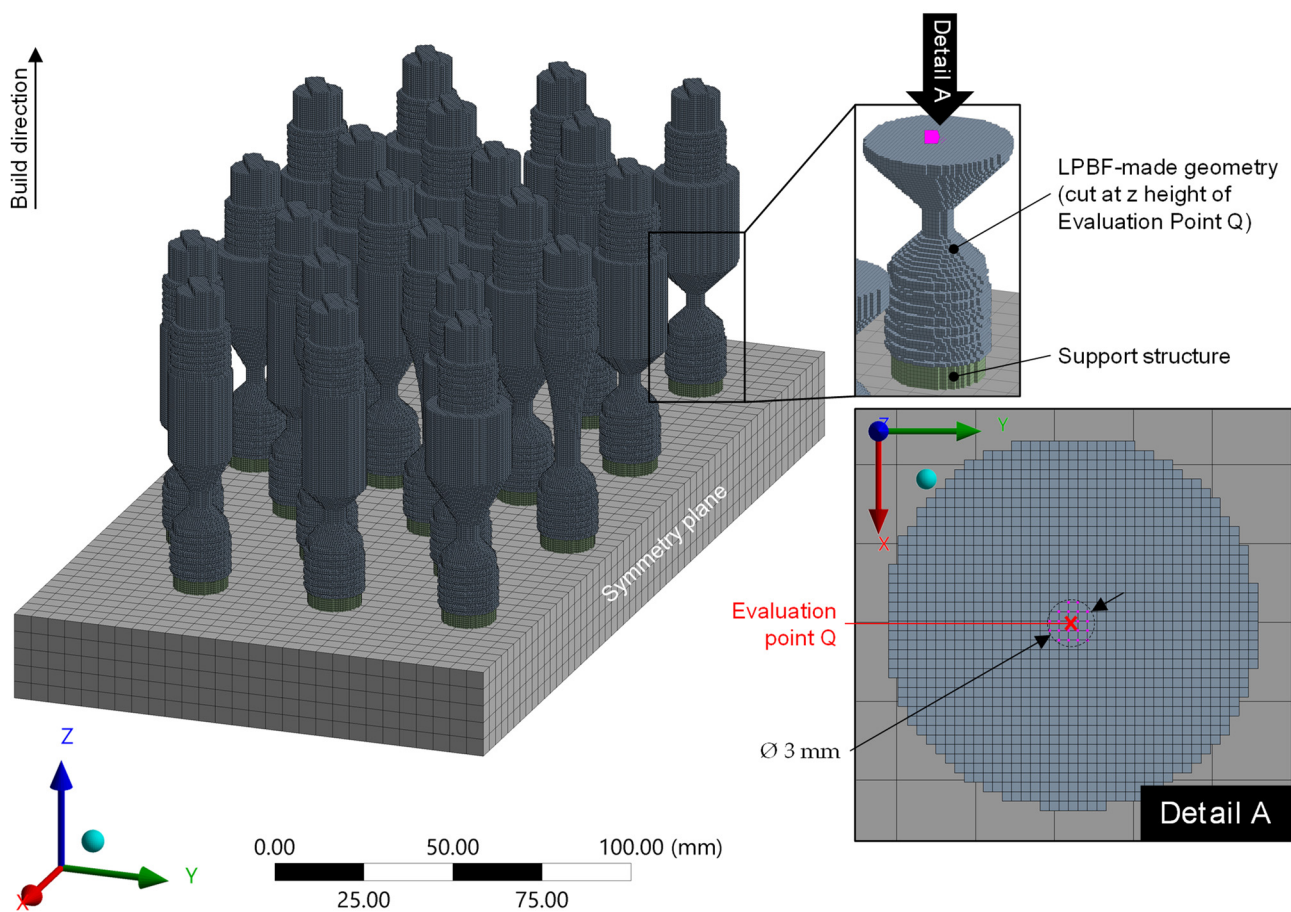


Figure 5. Sample arrangement in thermal simulation model of geometry variants Geo-a–Geo-u for tensile testing, Detail A showing evaluated node selection around evaluation point Q enclosed in respective tensile test sample diameter of 3 mm.

The simulated thermal histories of the geometry variants Geo-a–Geo-u were processed in Python 3 (Python Software Foundation, Wilmington, DE, USA) with the Pandas library in Jupyter Notebook to extract characteristic geometry-dependent parameters. Statistical software Centurion 18 (Statgraphics Technologies Inc., The Plains, VA, USA) was used to correlate the extracted parameters with the experimental results from the tensile tests.

3. Results and Discussion

3.1. Geometry Effect on Microstructure

Figure 6a,b show the microstructure of samples Geo-A and Geo-B at evaluation point P. For Geo-A, the martensitic α' phase is recognizable that is common for LPBF-manufactured Ti-6Al-4V in as built condition (Figure 6a). Geo-B, on the other hand, shows a microstructure with α lamellae embedded in a β matrix (Figure 6b). The EDS mapping confirms this finding because the lamellae show an increased Al content, indicating the α phase. The matrix shows increased vanadium concentration, which is characteristic for β phase. It is noted that an effect of the sample geometry exists that leads to significantly different microstructure evolution at the examination point P.

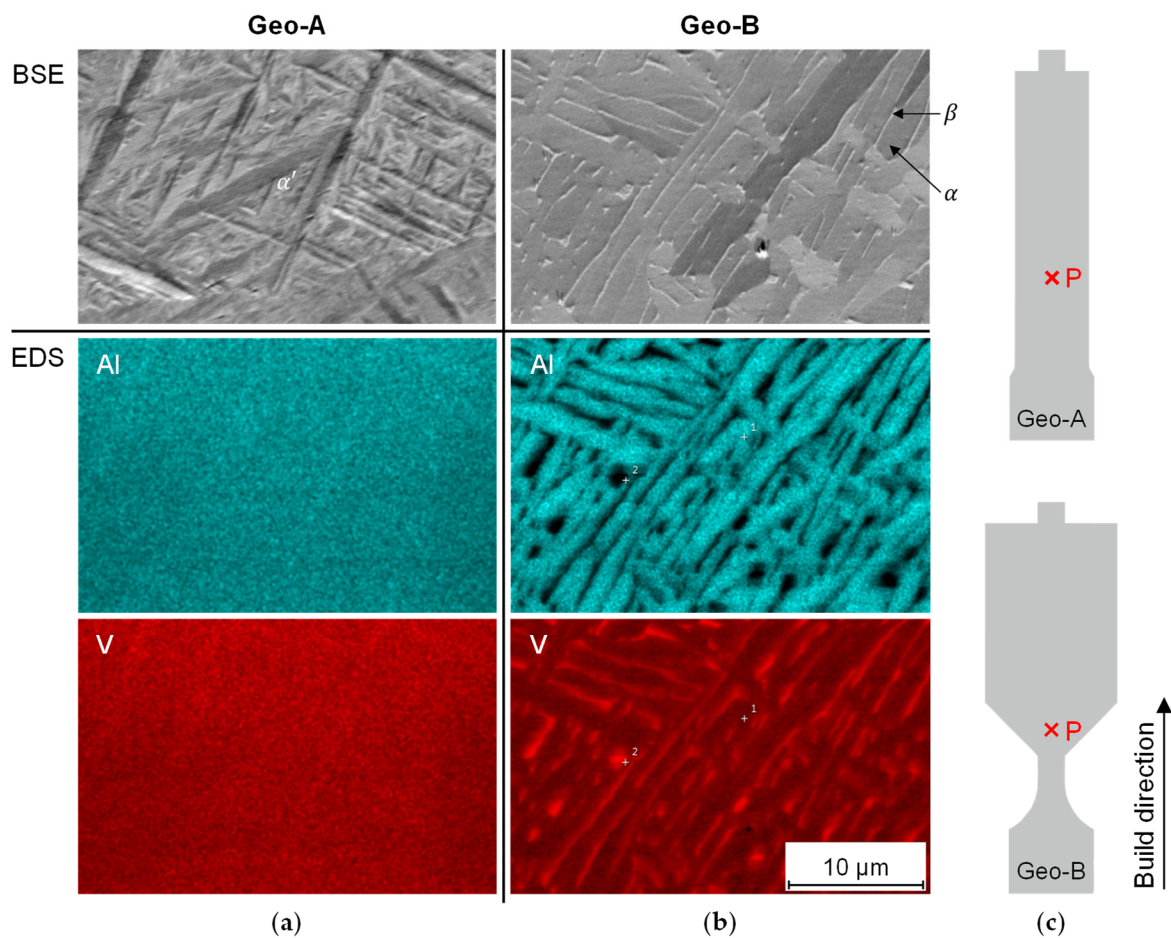


Figure 6. SEM images acquired in BSE mode and EDS element mapping of Al and V at evaluation point P for (a) Geo-A showing the martensitic α' microstructure and (b) Geo-B showing $\alpha + \beta$ microstructure, (c) Geometry variants Geo-A and Geo-B with evaluation point P marked.

Since a geometry-related difference in microstructure was found, the region vertically adjacent to point P was analyzed for Geo-B that is characterized by an unsteady cross section course (Figure 7a). Figure 7b shows exemplary SEM images of the microstructure at different vertical distances to point P dz_p . Phase fractions were determined from the BSE images by use of Weka segmentation (Figure 7c). At a vertical distance to point P of $dz_p = -3$ mm β matrix appears initially by a phase fraction of 2.797% (Figure 7c red). With progressing build job and increasing geometrical cross-section, β fraction continues to increase until it reaches a maximum of 23.716% at $dz_p = 1$ mm. From this height, the increased beta fraction remains approximately constant with increasing height and levels off at about 20%. At a height of $dz_p = 3$ mm a clearly formed lamellar $\alpha + \beta$ microstructure is observed. The results show that a completely different microstructure can exist in LPBF-made parts of Ti-6Al-4V in only 5 mm difference in build height. Only influenced by the sample geometry, a change from an almost martensitic α' microstructure to a lamellar $\alpha + \beta$ microstructure occurred. The observed α' microstructure in geometric areas not exposed to increased thermal input from heat accumulation or intrinsic heat treatment are in agreement with various studies, e.g., [4,13,21–24].

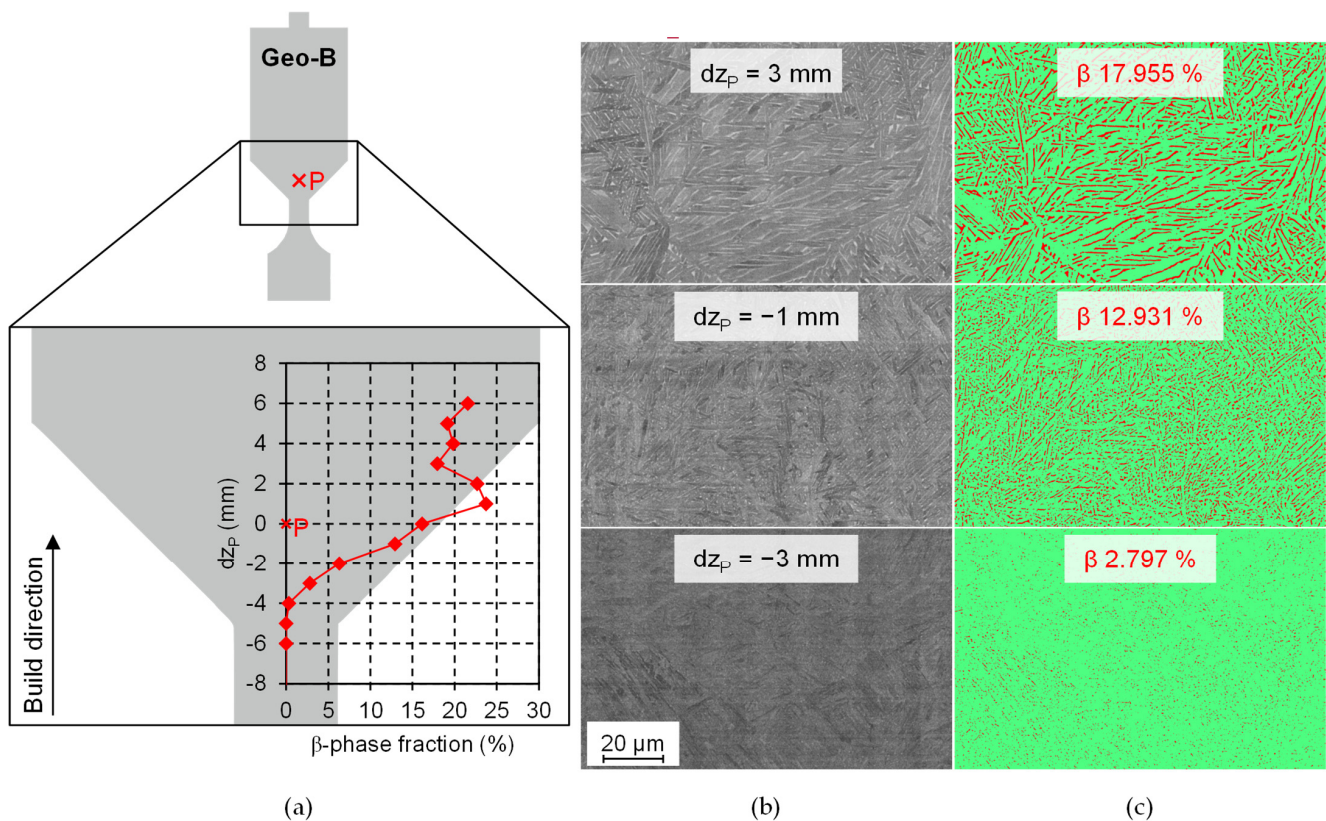


Figure 7. Geometry effect on microstructure for geometry variant Geo-B, (a) β phase fraction as a function of distance to point P in build-up direction dz_P , (b) SEM BSE images at $dz_P = -3, -1$ and 3 mm, (c) α (green)/ β (red) phase fractions separated by Weka segmentation.

In [3], decomposition with increased beta content of 4–6% was found in areas on the bottom side of the part (downskin), which is attributed to a locally increased local heat input. This corresponds to the observed decomposition found in this study at areas with rapidly increasing cross-sectional areas but with significantly higher beta content of ~20% in the present work. The higher beta amount could be due to the fact that lower surrounding solid volume is present with the used sample design, compared to a larger solid material amount of the part design used in [3]. This may lead to comparatively lower cooling rates and intrinsic heat treatment with longer duration at higher temperature levels. The $\alpha + \beta$ phase distribution in areas of locally increased thermal input observed in this study are similar to the observed microstructure in studies, where $\alpha + \beta$ microstructures were realized by in situ martensite decomposition via focal offset distance [8] or reduced inter layer time [25] even in primitive geometries. Consequently, it can be stated that the intrinsic heat treatment strongly affects the microstructure variation, driven by the geometry of the sample.

3.2. Geometry Effect on Mechanical Properties

3.2.1. Geometry Effect on Fatigue Properties

To mechanically characterize the microstructure at test point P that was found to be different for Geo-A and Geo-B, fatigue test samples were extracted from the LPBF-manufactured geometry variants (Figure 2a,b). After fatigue testing, the fracture surfaces were analyzed according to Section 2.5 to exclude those samples with a process-induced defect as crack origin from the generation of the S-N curve. In fatigue testing with stress ratio $R = 0.1$, it is noticeable that Geo-A shows significantly higher fatigue life over several stress levels than Geo-B (Figure 8b). With respect to the observed microstructures in point P for the two geometry variants (Figure 8a), it can be stated that a deviation from the common

α' microstructure in LPBF in the form of an $\alpha + \beta$ phase distribution leads to lower fatigue life. This is in line with other investigations that find that a martensitic α' phase leads to superior fatigue life due to a high density of dislocations [24]. It is noticeable that more than twice as many samples from Geo-A are excluded from the test evaluation due to a crack origin at a pore. This could be explained by the fact that the strength of the microstructure of Geo-B was so strongly reduced by the intrinsic heat treatment that these phases represent an even weaker point than regions with pores and reduced IHT influence leading to the failure in solid material. In contrast, the pores in Geo-A may represent the weakest areas compared to the strong fully martensitic α' Phase and therefore act as crack initiation site.

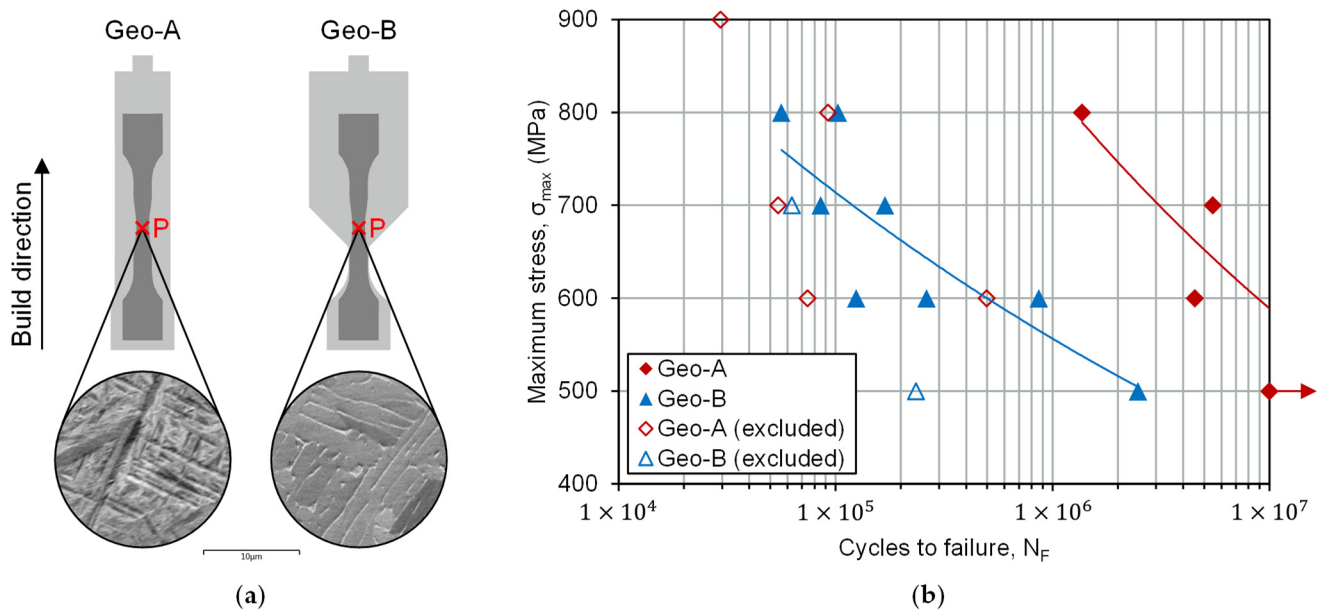


Figure 8. Geometry effect on fatigue life based on geometry variants Geo-A and Geo-B, (a) Geo-A and Geo-B with corresponding microstructure at evaluation point P, (b) Fatigue life of Geo-A and Geo-B, $R = 0.1$, samples with crack initiation at pore defects excluded (unfilled data points).

3.2.2. Geometry Effect on Ultimate Tensile Strength

To understand the geometry effect on mechanical properties for a broader range of geometries, the geometry variants from Table 1 were manufactured by LPBF, varying the geometric parameters that are described in Figure 3. After machining to a uniform geometry, tensile testing was carried out. It was found that the samples with the more gently increasing cross-sectional area and therefore lower thermal input (Geo-s–Geo-u) showed the highest ultimate tensile strength UTS of around 1300 MPa (Figure 9). For samples with an overhang angle $\delta = 45^\circ$, there is a trend that UTS decreases with increasing upper diameter D . This can be explained by the fact that with increasing diameter D the heat input at point P increases and thus the phase transformation $\alpha' \rightarrow \alpha + \beta$ becomes more apparent. Further correlations cannot be interpreted from the results due to the scatter of measured values.

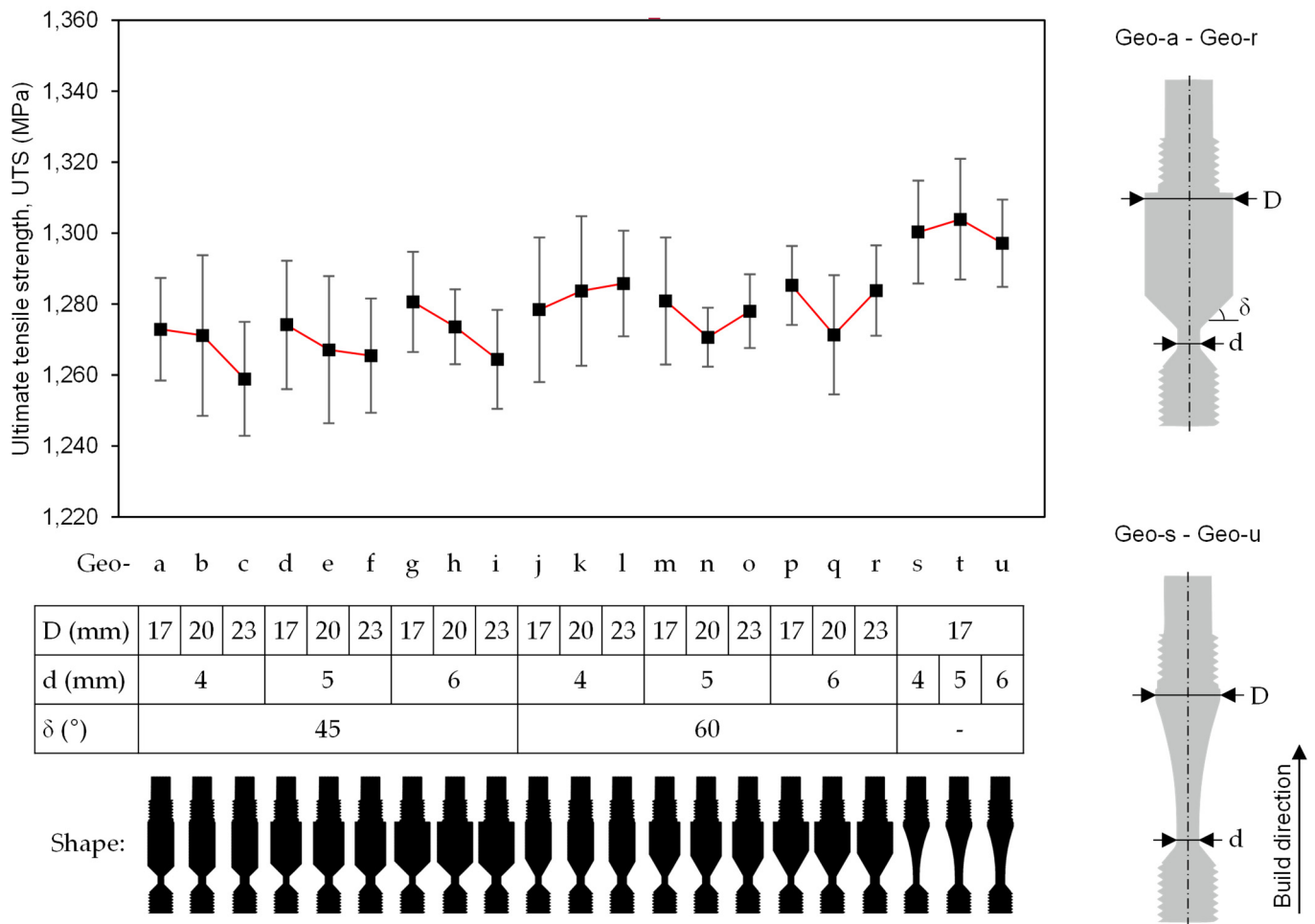


Figure 9. Ultimate tensile strength of geometry variants Geo-a–Geo-u with associated shape (black) and geometrical parameters indicated on the right.

The observations show that faster increasing of cross-sectional areas in the build-up direction not only leads to lower fatigue life according to Section 3.2.2 but also to lower UTS. This is in line with [24], since the martensitic α' phase leads to high strength, what is expected to be present at higher fraction in Geo-s–Geo-u, according to the findings in Section 3.1. Other studies [7,8,25–27] aim to avoid the martensitic α' phase and instead achieve an $\alpha + \beta$ microstructure with the motivation to obtain more favorable material properties in this way. The results achieved in this work indicate that the martensitic α' as built microstructure with lower heat input leads to the highest static and dynamic strengths. Despite the fact that no fracture toughness was characterized here, for which an $\alpha + \beta$ phase distribution is more advantageous in general, it can still be stated that for applications where high static or dynamic strength is required, the martensitic α' phase could be the preferred microstructure. Depending on the application, a deviation from the α' phase can therefore be considered a potentially undesirable property, whose prediction is thus highly relevant for LPBF-manufactured parts. Furthermore, with knowledge of the individual phases and the associated mechanical properties in complex parts, heat treatments can be omitted if the predicted material properties are already known and can be considered in the design process.

3.3. Simulation of Thermal History

The sample variants used in the tensile test were simulated according to Section 2.6 and the time-temperature-curves (thermal histories) at the nodes around point Q of the variant were evaluated. Figure 10 shows thermal histories of two contrary geometry variants. At

time 9306.8 s, the element layer in which the evaluated nodes are located n_Q is generated in both cases. According to the super layer approach of the applied simulation, the nodes are heated to melting temperature (1605 °C). Immediately afterwards, the temperature curve drops comparatively steeply according to the high cooling rate in LPBF, before the following element layer is applied, whose nodes are also heated to melting temperature. Because the nodes at the bottom of this following layer are at the same time the upper nodes of the evaluated layer n_Q at point Q, the temperature rises again to melting temperature. In the following phase, the temperature at the nodes decreases depending on the geometry, so that a characteristic thermal history results for each geometry variant.

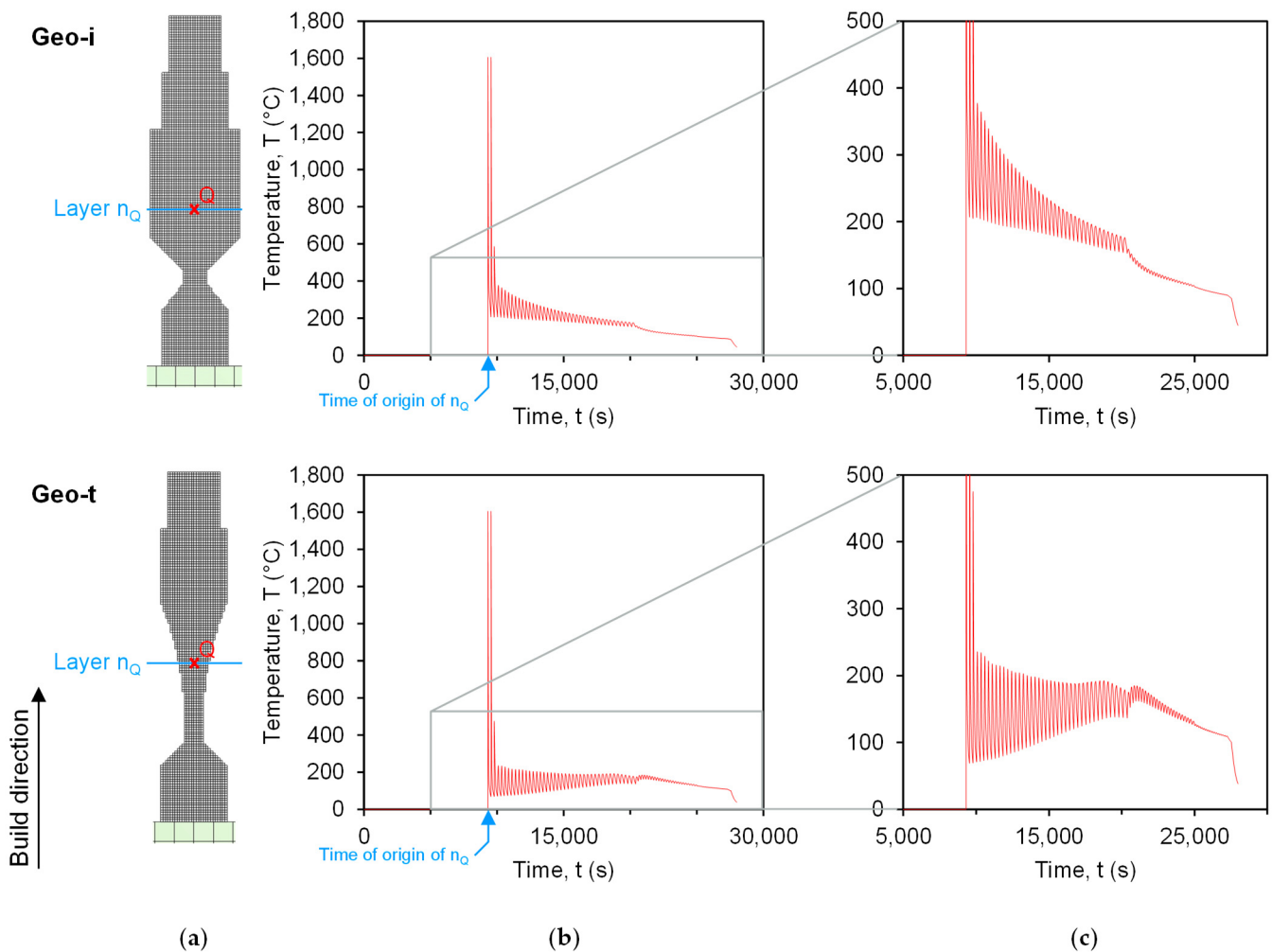


Figure 10. (a) Exemplary geometry variants Geo-i and Geo-t with evaluation point Q in corresponding layer n_Q , (b) Time-temperature profile (thermal history) at Q with time of origin of marked layer n_Q , (c) enlarged section of the thermal history at Q.

Comparing the contrary geometry variants in Figure 10, it can be seen that Geo-i with a more rapidly increasing cross-sectional area in the build-up direction leads to an overall higher temperature history than Geo-t with a more gentle cross-sectional area increase. While the thermal history of Geo-i decreases continuously with increasing time, the temperature of Geo-t remains at a lower level in a band between approximately 80 °C and 200 °C. Furthermore, there is a secondary rise in Geo-t that occurs after the cross section of Geo-t reaches a maximum at about 20,000 s. This can be explained by the abruptly shortened inter layer time at this point, which occurs because the enlarged cross section of the one sample type, such as Geo-i, ends and is followed by a section with a smaller cross section. This leads to a shorter scan time of the entire layer in the LPBF process

and thus reduces the inter layer time, which in turn leads to a reduction in the cooling time and thus to a buildup of heat. As time proceeds, the temperature curve decreases again because the distance of the deposited layers from point Q increases continuously.

Even though in the real LPBF process temperatures far above the melting temperature are reached, the use of the melting temperature in the selected approach has proven to be appropriate because the focus is on the thermal history in the solid material state with temperatures that are always below the melting temperature. The identified differences in the thermal histories of the sample variants show that the geometry effect is represented in the selected simulation approach. The simulation of the 21 geometry variants at the same time is, with a simulation time of 9.26 h on an average desktop workstation (Intel Core i9-7920X CPU @ 2.9 GHz, 14.323 GB RAM usage), much more efficient than conventional simulations that allow predictions of the microstructure, such as phase field simulations or cellular automata, but which are not applicable for the simulation of entire parts due to high computational effort [15]. In case the results of the thermal simulations used in this work allow a statement on the emerging microstructure, the opportunity for the estimation of the mechanical behavior of entire parts would arise for the first time ever.

3.4. Correlation between Mechanical Properties and Simulated Thermal History

A phenomenological approach was chosen to quantify and discretize the thermal histories of the 21 different geometry variants that resulted from thermal simulation. For this purpose, the integral of the temperature at the examination point Q from build job start time t_{start} to end time t_{end} was calculated that equals the area A under the time-temperature curve (1).

$$\int_{t_{\text{start}}}^{t_{\text{end}}} T = A \quad (1)$$

Figure 11a shows as an example the thermal history of Geo-i. To take the effect of temperature height on microstructure evolution into account, A was divided into n_p partitions of different temperature intervals ΔT_p , allowing considering them individually (Figure 11b). The resulting partition areas A_n were used as independent variables in a linear multiple regression to correlate with the estimated ultimate tensile strength

$$U\hat{T}S = C + \sum_{i=1}^{n_p} \beta_i * A_i \quad (2)$$

as dependent variable with a constant factor C and coefficients β_i for each corresponding partition A_i . When examining the partition areas A_n with $\Delta T_p = 50^\circ\text{C}$ and $\Delta T_p = 100^\circ\text{C}$, it was found that partitions in the temperature range $> 700^\circ\text{C}$ are statistically not usable for modeling. This may result from the fact that the geometry dependence above this temperature range does not affect the simulated thermal history with the chosen approach.

Geo-i

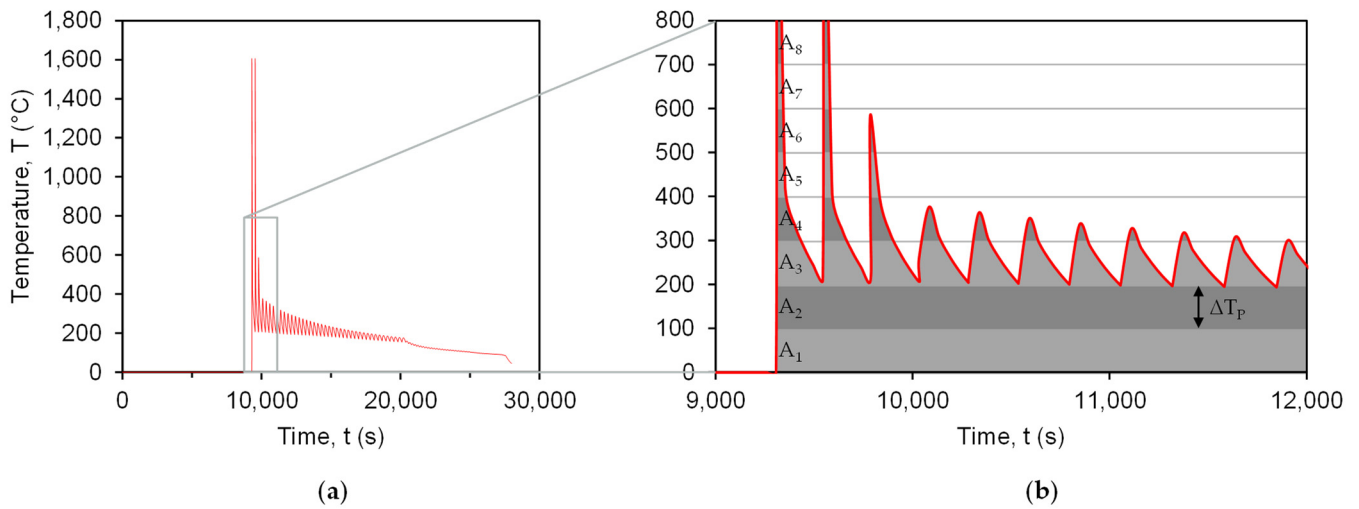


Figure 11. (a) Thermal history of Geo-i at evaluation point Q, (b) enlarged section of the thermal history with area under the time temperature curve subdivided into partitions A₁–A₈ of width $\Delta T_P = 100$ °C.

Table 3 shows the statistical evaluation parameters coefficient of determination R^2 , adjusted coefficient of determination R^2_{adj} and standard error SE for the several linear multiple regressions performed with $\Delta T_P = 50$ °C, “x” indicating which partitions and therefore temperature ranges were considered in the respective regression model.

Table 3. Series of multiple linear regression studies between ultimate tensile strength and partitions from simulated thermal history with varied number of partitions considered, red coloring means lowest value and green coloring means highest value of the respective value per row.

Partition	Temperature Range (°C)	Consideration in Model (x = Yes)									
A ₁	0–50	x	-	-	-	-	-	-	-	-	-
A ₂	50–100	x	x	-	-	-	-	-	-	-	-
A ₃	100–150	x	x	x	-	-	-	-	-	-	-
A ₄	150–200	x	x	x	x	-	-	-	-	-	-
A ₅	200–250	x	x	x	x	x	-	-	-	-	-
A ₆	250–300	x	x	x	x	x	x	-	-	-	-
A ₇	300–350	x	x	x	x	x	x	x	-	-	-
A ₈	350–400	x	x	x	x	x	x	x	x	-	-
A ₉	400–450	x	x	x	x	x	x	x	x	x	-
A ₁₀	450–500	x	x	x	x	x	x	x	x	x	x
A ₁₁	500–550	x	x	x	x	x	x	x	x	x	x
A ₁₂	550–600	x	x	x	x	x	x	x	x	x	x
A ₁₃	600–650	x	x	x	x	x	x	x	x	x	x
A ₁₄	650–700	x	x	x	x	x	x	x	x	x	x
Number of partitions n_P		14	13	12	11	10	9	8	7	6	5
Coefficient of determination R^2 (%)		94.81	94.14	94.14	94.13	94.08	93.48	93.26	93.21	88.14	78.19
Adj. coeff. of det. R^2_{adj} (%)		82.69	83.27	85.34	86.94	88.16	88.15	88.77	89.55	83.06	70.92
Standard error SE (MPa)		4.885	4.803	4.495	4.243	4.040	4.043	3.936	3.795	4.834	6.332

Figure 12a shows the statistical parameters from Table 3 in relation to the number of considered partitions n_P . It can be seen that the highest adjusted coefficient of determination $R^2_{adj} = 89.55\%$ and lowest standard error $SE = 3.795$ MPa were identified at $n_P = 7$ partitions with considered temperature ranges starting from 350 °C. Further increasing of n_P does neither increase R^2_{adj} nor reduce SE . For predicting the ultimate tensile strengths

based on the thermal simulation results, the following approximate Equation (3) with $n_p = 7$ was determined for the expected tensile strength:

$$\begin{aligned} U\hat{T}S = & (1016.97 + 0.00338287 \times A_8 - 0.00712774 \times A_9 - 0.0576664 \times A_{10} + 0.00077465 \times A_{11} \\ & - 0.0122671 \times A_{12} - 0.376996 \times A_{13} + 0.572771 \times A_{14}) \text{ MPa} \end{aligned} \quad (3)$$

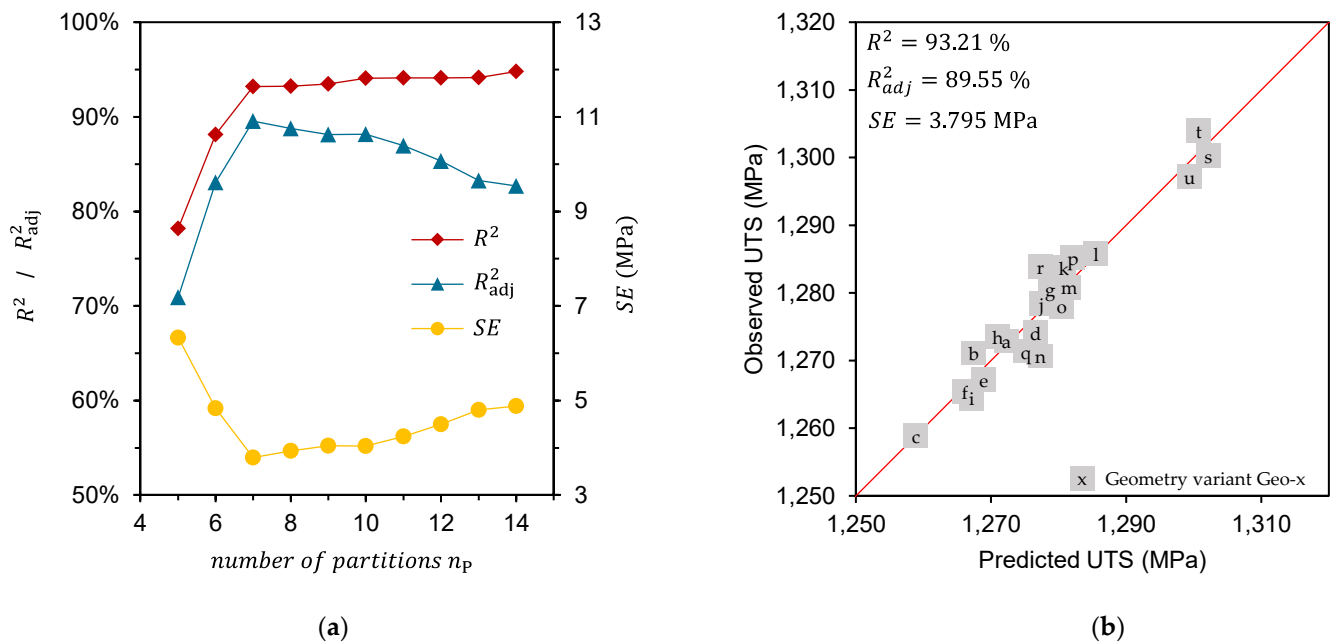


Figure 12. (a) Coefficient of determination R^2 , adjusted coefficient of determination R^2_{adj} and standard error SE depending on the number of considered partitions in the regression n_p , (b) Prediction accuracy of the correlation model based on Equation (3) with geometry variants Geo-a–Geo-u.

It is noticeable that the highest prediction accuracy of the ultimate tensile strength is present in a regression model with temperature ranges above 350 °C. This can be explained by the fact that martensite decomposition only takes place at temperatures above approx. 400 °C [8]. Lower temperatures have no effect on the microstructure formation. Figure 12b shows the prediction accuracy of the correlation model Equation (3), with the predicted ultimate tensile strength (UTS) plotted on the horizontal axis and the observed UTS on the vertical axis for the 21 investigated geometries.

Figure 12b clearly shows that all three geometry variants Geo-s, Geo-t and Geo-u with the more gently increasing cross-sectional areas achieve the highest ultimate tensile strengths both in the experiment (observed UTS) and in the correlation equation (predicted UTS). Furthermore, with an adjusted coefficient of determination $R^2_{adj} = 89.55\%$, it is evident that for the investigated geometry variants UTS can be linearly correlated with parameters from the thermal history simulated with the computationally resource-saving super layer approach.

4. Conclusions

In the present work, the effect of geometry on the material properties of LPBF-made parts from Ti-6Al-4V was investigated. A phenomenological approach is presented to correlate ultimate tensile strength with results from highly efficient simplified LPBF thermal simulations, which are in principle applicable at part level with an increased database. For the experimental investigation of local sample regions, a methodology was developed, which allows studying the geometry influence on the resulting microstructure in isolation. Transient thermal simulations of the LPBF process were performed using the super layer approach. The resulting time-temperature curves (thermal histories) were evaluated at

the locations of the samples where they are mechanically characterized in the experiment. For geometric sample variations, differences in the resulting microstructure were found. In detail, areas exposed to impeded heat dissipation and therefore higher local thermal input over time show an $\alpha + \beta$ phase distribution with a β fraction of up to 20% compared to the common α' microstructure in areas not exposed to excessive thermal input. These differences are found even for areas only 5 mm apart from each other in build-up direction and result in reduced ultimate tensile strength and fatigue life. From the thermal simulations with simplified super layer approach, the integrals of the time-temperature curves were calculated and correlated with the ultimate tensile strength. Based on data from 21 different geometry variants, a correlation model was successfully established with an adjusted coefficient of determination of 89.55%. This work demonstrated that for the selected sample geometries, a correlation is possible between the mechanical properties and computational resource-saving simulations that are theoretically feasible at part scale. This proof of concept provides the basis for an efficient prediction model of the mechanical performance of additively manufactured part applications for the first time. However, to enable the model to be applied to real part designs it has to be extended in future work in terms of the database and the parameters that are extracted from the thermal simulations to make it universally applicable. The finding that within a difference of only 5 mm in build height, a completely contrary microstructure is present, which only results from the part geometry, should raise the awareness of LPBF users to give greater importance to the topic of part geometry. In industrial practice, to avoid these inhomogeneities, additional support structures can be applied in overheated part areas to prevent intrinsic heat treatment. Until the present model is universally applicable to part geometries in future, heat treatment and extensive testing should always be considered for critical part applications made of Ti-6Al-4V by use of LPBF.

Author Contributions: Conceptualization, J.M.; methodology, J.M.; software, J.M. and T.S.; validation, J.M., T.S. and E.B.; writing—original draft preparation, J.M.; writing—review and editing, J.M., E.B., N.P. and C.H.; visualization, J.M.; supervision, C.H. All authors have read and agreed to the published version of the manuscript.

Funding: This research received no external funding.

Data Availability Statement: The data presented in this study are available on request from the corresponding author.

Conflicts of Interest: The authors declare no conflict of interest.

References

1. Berrocal, L.; Fernández, R.; González, S.; Periñán, A.; Tudela, S.; Vilanova, J.; Rubio, L.; Martín Márquez, J.M.; Guerrero, J.; Lasagni, F. Topology optimization and additive manufacturing for aerospace components. *Prog. Addit. Manuf.* **2019**, *4*, 83–95. [[CrossRef](#)]
2. Chahal, V.; Taylor, R.M. A review of geometric sensitivities in laser metal 3D printing. *Virtual Phys. Prototyp.* **2020**, *15*, 227–241. [[CrossRef](#)]
3. Barriobero-Vila, P.; Artzt, K.; Stark, A.; Schell, N.; Siggel, M.; Gussone, J.; Kleinert, J.; Kitsche, W.; Requena, G.; Haubrich, J. Mapping the geometry of Ti-6Al-4V: From martensite decomposition to localized spheroidization during selective laser melting. *Scr. Mater.* **2020**, *182*, 48–52. [[CrossRef](#)]
4. Zhao, C.; Fezzaa, K.; Cunningham, R.W.; Wen, H.; de Carlo, F.; Chen, L.; Rollett, A.D.; Sun, T. Real-time monitoring of laser powder bed fusion process using high-speed X-ray imaging and diffraction. *Sci. Rep.* **2017**, *7*, 3602. [[CrossRef](#)] [[PubMed](#)]
5. Longhitano, G.A.; Larosa, M.A.; Jardini, A.L.; Zavaglia, C.A.d.C.; Ierardi, M.C.F. Correlation between microstructures and mechanical properties under tensile and compression tests of heat-treated Ti-6Al-4 V ELI alloy produced by additive manufacturing for biomedical applications. *J. Mater. Process. Technol.* **2018**, *252*, 202–210. [[CrossRef](#)]
6. Erdakov, I.; Glebov, L.; Pashkeev, K.; Bykov, V.; Bryk, A.; Lezin, V.; Radionova, L. Effect of the Ti6Al4V Alloy Track Trajectories on Mechanical Properties in Direct Metal Deposition. *Machines* **2020**, *8*, 79. [[CrossRef](#)]
7. Barriobero-Vila, P.; Gussone, J.; Haubrich, J.; Sandlöbes, S.; Da Silva, J.C.; Cloetens, P.; Schell, N.; Requena, G. Inducing Stable $\alpha + \beta$ Microstructures during Selective Laser Melting of Ti-6Al-4V Using Intensified Intrinsic Heat Treatments. *Materials* **2017**, *10*, 268. [[CrossRef](#)] [[PubMed](#)]

8. Xu, W.; Brandt, M.; Sun, S.; Elambasseril, J.; Liu, Q.; Latham, K.; Xia, K.; Qian, M. Additive manufacturing of strong and ductile Ti–6Al–4V by selective laser melting via in situ martensite decomposition. *Acta Mater.* **2015**, *85*, 74–84. [[CrossRef](#)]
9. Sieniawski, J.; Ziaja, W.; Kubiak, K.; Motyk, M. Microstructure and Mechanical Properties of High Strength Two-Phase Titanium Alloys. In *Titanium Alloys—Advances in Properties Control*; Sieniawski, J., Ziaja, W., Eds.; InTech: Rijeka, Croatia, 2014; ISBN 978-953-51-1110-8.
10. Wei, H.L.; Mukherjee, T.; Zhang, W.; Zuback, J.S.; Knapp, G.L.; De, A.; DebRoy, T. Mechanistic models for additive manufacturing of metallic components. *Prog. Mater. Sci.* **2021**, *116*, 100703. [[CrossRef](#)]
11. Körner, C.; Markl, M.; Koepf, J.A. Modeling and Simulation of Microstructure Evolution for Additive Manufacturing of Metals: A Critical Review. *Met. Mater. Trans. A* **2020**, *51*, 4970–4983. [[CrossRef](#)]
12. Nandwana, P.; Plotkowski, A.; Kannan, R.; Yoder, S.; Dehoff, R. Predicting geometric influences in metal additive manufacturing. *Mater. Today Commun.* **2020**, *25*, 101174. [[CrossRef](#)]
13. Pantawane, M.V.; Ho, Y.-H.; Joshi, S.S.; Dahotre, N.B. Computational Assessment of Thermokinetics and Associated Microstructural Evolution in Laser Powder Bed Fusion Manufacturing of Ti6Al4V Alloy. *Sci. Rep.* **2020**, *10*, 7579. [[CrossRef](#)] [[PubMed](#)]
14. Liang, H.; Xie, D.; Mao, Y.; Shi, J.; Wang, C.; Shen, L.; Tian, Z. The Size Effect on Forming Quality of Ti–6Al–4V Solid Struts Fabricated via Laser Powder Bed Fusion. *Metals* **2019**, *9*, 416. [[CrossRef](#)]
15. Shrestha, R.; Shamsaei, N.; Seifi, M.; Phan, N. An investigation into specimen property to part performance relationships for laser beam powder bed fusion additive manufacturing. *Addit. Manuf.* **2019**, *29*, 100807. [[CrossRef](#)]
16. Leicht, A.; Klement, U.; Hryha, E. Effect of build geometry on the microstructural development of 316L parts produced by additive manufacturing. *Materials Characterization. Mater. Charact.* **2018**, *143*, 137–143. [[CrossRef](#)]
17. Walker, J.R. Multi-Sensor Approach to Determine the Effect of Geometry on Microstructure in Additive Manufacturing. 2019. Available online: https://corescholar.libraries.wright.edu/etd_all/2145 (accessed on 27 January 2022).
18. Promoppatum, P.; Yao, S.-C.; Pistorius, P.C.; Rollett, A.D.; Coutts, P.J.; Lia, F.; Martukanitz, R. Numerical modeling and experimental validation of thermal history and microstructure for additive manufacturing of an Inconel 718 product. *Prog. Addit. Manuf.* **2018**, *3*, 15–32. [[CrossRef](#)]
19. Nitzler, J.; Meier, C.; Müller, K.W.; Wall, W.A.; Hodge, N.E. A novel physics-based and data-supported microstructure model for part-scale simulation of laser powder bed fusion of Ti–6Al–4V. *Adv. Model. Simul. Eng. Sci.* **2021**, *8*, 1–39. [[CrossRef](#)]
20. Martin, A.A.; Calt, N.P.; Khairallah, S.A.; Wang, J.; Depond, P.J.; Fong, A.Y.; Thampy, V.; Guss, G.M.; Kiss, A.M.; Stone, K.H.; et al. Dynamics of pore formation during laser powder bed fusion additive manufacturing. *Nat. Commun.* **2019**, *10*, 1987. [[CrossRef](#)]
21. Liu, S.; Shin, Y.C. Additive manufacturing of Ti6Al4V alloy: A review. *Mater. Des.* **2019**, *164*, 107552. [[CrossRef](#)]
22. Vanmeensel, K.; Lietaert, K.; Vrancken, B.; Dadbakhsh, S.; Li, X.; Kruth, J.-P.; Krakhmalev, P.; Yadroitsev, I.; van Humbeeck, J. Additively manufactured metals for medical applications. In *Additive Manufacturing*; Elsevier: Amsterdam, The Netherlands, 2018; pp. 261–309. ISBN 9780128121559.
23. Thijs, L.; Verhaeghe, F.; Craeghs, T.; van Humbeeck, J.; Kruth, J.-P. A study of the microstructural evolution during selective laser melting of Ti–6Al–4V. *Acta Mater.* **2010**, *58*, 3303–3312. [[CrossRef](#)]
24. Rafi, H.K.; Karthik, N.V.; Gong, H.; Starr, T.L.; Stucker, B.E. Microstructures and Mechanical Properties of Ti6Al4V Parts Fabricated by Selective Laser Melting and Electron Beam Melting. *J. Mater. Eng. Perform.* **2013**, *22*, 3872–3883. [[CrossRef](#)]
25. Lui, E.W.; Xu, W.; Pateras, A.; Qian, M.; Brandt, M. New Development in Selective Laser Melting of Ti–6Al–4V: A Wider Processing Window for the Achievement of Fully Lamellar $\alpha + \beta$ Microstructures. *JOM* **2017**, *69*, 2679–2683. [[CrossRef](#)]
26. Sallica-Leva, E.; Caram, R.; Jardini, A.L.; Fogagnolo, J.B. Ductility improvement due to martensite α' decomposition in porous Ti–6Al–4V parts produced by selective laser melting for orthopedic implants. *J. Mech. Behav. Biomed. Mater.* **2016**, *54*, 149–158. [[CrossRef](#)] [[PubMed](#)]
27. Ali, H.; Le, M.; Ghadbeigi, H.; Mumtaz, K. In-situ residual stress reduction, martensitic decomposition and mechanical properties enhancement through high temperature powder bed pre-heating of Selective Laser Melted Ti6Al4V. *Mater. Sci. Eng. A* **2017**, *695*, 211–220. [[CrossRef](#)]